ROYAL SOCIETY OF CHEMISTRY

PAPER

Check for updates

Surface tailoring of porphyrin *via* phosphorus-doping and chromium encapsulation towards the detection of CO_2, SO_2, and NO_2 gas pollutants: a computational study

Ededet A. Eno, *[a] Miracle N. Ogbogu,[b] Morenikeji A. Ajayi,[c] Mojirade Mafimisebi,[d] Jeremiah E. Ochepo,[e] Opeyemi M. Oyebanji, [iD] *[c] Chinyere Chukwu Phoebe[a] and Ernest G. Irilochuwe[f]

As burning of fossil fuels is a major contributor to air pollution, as a result, both acute and chronic releases of these toxic chemical gases into the air can cause significant damage to the cardiovascular and pulmonary systems, potentially leading to death. This therefore calls for environmental remediation, through the detection of these gases, since they cannot be completely eradicated from the atmosphere. Herein, this research presents a newly tailored phosphorus-doped chromium encapsulation porphyrin (P–Cr@PPR) for the detection of CO_2, SO_2, and NO_2 gas pollutants. The potential of this material as a suitable detector for these gases was studied through various computational analyses, carried out using the DFT/HSEH1PBE/LANL2DZ level of theory. Due to interaction, slight changes in the surface morphology were observed, showing the effect of detection on the surface. All systems showcased high perturbation energy, with the greatest perturbation energies of 909.58 and 481.60 kcal mol^{-1} observed for the surface upon the adsorption of SO_2 gas, showing that the Cr–P@PPR–SO_2 complex will be easily stabilized as compared to its counterparts studied. Majorly, slight changes in the surface morphology show the effect of the detection of the surface. Among the systems, non-covalent and partial covalent forms of interactions were observed, with a positive value of ellipticity (ε) showing some degree of ionic character with greater ionic contribution. Lastly, detecting strength follows an increasing order of: NO_2–Cr–P@PPR < SO_2–Cr–P@PPR < CO_2–Cr–P@PPR, with the detection energies recorded as 10.471, 6.503, and 4.581 eV, respectively. Based on the characteristic properties exhibited by this material, it can be a potential candidate to be considered when selecting a material to engineer a detection device for these gas pollutants.

[a]Department of Pure and Applied Chemistry, University of Calabar, Nigeria. E-mail: dialededet@yahoo.com

[b]Department of Genetics and Biotechnology, University of Calabar, Nigeria

[c]Department of Chemistry, University of Ibadan, Nigeria. E-mail: oyebanjimorakinyo@gmail.com

[d]Department of Chemistry, Adekunle Ajasin University, Akungba Akoko, Nigeria

[e]Department of Computer Science, Fitchburg State University, Massachusetts, USA

[f]Department of Microbiology, University of Calabar, Nigeria

1 Introduction

Human activities significantly contribute to air pollution through various sources like burning, smoking, and industrial processes. This pollution is caused by harmful gases like CO_2, SO_2, and NO_2, amongst others, posing a significant threat to human health and the environment.[1–3] These gases originate from various sources, including domestic appliances, power plants, and burning fossil fuels.[4,5] They can cause respiratory problems, acid rain, and contribute to climate change.[6]

Nitrogen dioxide (NO_2), sulfur dioxide (SO_2), and carbon monoxide (CO) are some of the important gases that serve as ambient air pollutants. Exposure to these gases, particularly NO_2, can cause catastrophic injuries and even death in humans. It can also increase the risk of respiratory tract infections by weakening the immune system.[7,8] Sulfur dioxide (SO_2) can cause respiratory symptoms in patients, especially those with underlying pulmonary disease. Research shows that experimental exposure to SO_2 can lead to changes in airway physiology, including increased airway resistance.[9,10] Both acute and chronic releases of these toxic chemical gases into the air can cause significant damage to the cardiovascular and pulmonary systems, potentially leading to death. In addition, high concentrations of NO_2 in confined spaces can be extremely harmful, even fatal to humans.[11–13] Human activities, such as burning fossil fuels (coal, oil, and natural gas), are major contributors to air pollution, including CO_2 and NO_2 emissions.[14] Also, sulfur dioxide (SO_2) is known as a key component

of acid rain. When sulfuric acid falls as rain, it acidifies both aquatic and terrestrial ecosystems, harming plants and animals.[15,16] Due to their harmful effects, the need for environmental remediation brings about the detection of these gases.

Nanomaterials (where some call it a tiny powerhouse) are a fascinating class of materials with at least one dimension less than 100 nanometers.[17] From this, they are significantly smaller than microscale materials, which typically range from 1 to 100 micrometers. In simpler terms, nanomaterials are about one billionth of a meter in size.[18,19] These materials come in different shapes, namely: nanoparticles, nanorods, and nanosheets, amongst others.[20] Their dimensionality is often used in determining their classification, wherein zero-dimensional nanomaterials are called nanoparticles. In furtherance, these materials can be categorized distinctively based on their unique properties and structures: metal nanomaterials use divalent or trivalent metal ions as starting materials and can be prepared through various methods like chemical or photochemical techniques; semiconductor nanomaterials bridges the gap between metals and non-metals, these materials have wide band gaps that influence their properties when modified; polymeric nanomaterials encompasses nanocomposites, polymer nanoparticles, block copolymers, and dendrimers; and lastly carbon-based nanomaterials as the name suggests, are carbon-based and include fullerenes and carbon nanotubes.[21–23] Porphyrin, a molecule with just two nitrogen atoms linked by a carbon chain, is generating excitement as a powerful gas sensor. It is important to note that porphyrin can not only capture gases but also selectively choose its targets. Scientists are customizing its structure using different functional groups, like adding hydroxyl groups to attract SO_2 or alkyl chains for CO_2. This targeted approach is even being used to tackle a real-world problem: capturing harmful SO_2 emissions from industrial sources. Research by Gajjar and Roy (2024), studied gas sensing through transport characteristics and analyzed NH_3, SO_2, NO_2, and H_2O for adsorption of energy, charge density, and recovery time. Their findings indicate that the porphyrin's electronic transport changes significantly with gas adsorption. This suggests the potential for low-power, ultrasensitive, recyclable gas sensors using NEGF formalism and DFT.[24]

Various research has been conducted on the adsorption of CO_2, SO_2, and NO_2 gases on different nano surfaces. However, a few works have been done using the porphyrin surface for the adsorption of these gases. In an adsorption of carbon dioxide, ethane, and methane on porphyrin-based nanoporous organic polymers carried out by Jun Yan and team, a beneficial result towards designing and constructing better surfaces derived from tetrahedral-structured building blocks for simple molecular gas adsorption in the future.[25] In another study conducted by Yeongran *et al.* on gas capture and precious metal adsorption using alkyl-linked porphyrin porous polymers, inexpensive and scalable porous porphyrin polymers were found to offer great potential in capture, separation, and precious metal recovery.[26] Haang and Khang investigated the adsorption properties of the Sc_2CF_2 monolayer towards the adsorption of various gases, including CO_2, NO_2, and SO_2. It was found that the adsorption

of these gases does not change the conductive behavior of the monolayer. Also, the adsorption energy indicates that the monolayer exhibits low adsorption selectivity. This is due to the molecule's physiosorbed on the Sc_2CF_2 monolayer.[27] Furthermore, Saini and Pandey (2025) studied 5,10,15,20-tetrakis-(4-hydroxyphenyl)porphyrin (TPPH) and its nickel (NiTPPH) and zinc (ZnTPPH) forms as gas sensors for CO_2, $COCl_2$, CO, and HCN using density functional theory (DFT). The results show NiTPPH and ZnTPPH have strong affinity for CO_2 and $COCl_2$, with NiTPPH-$COCl_2$ having the most stable interaction (adsorption energy ~ 0.326 eV). Thus, both porphyrins are minimally sensitive to CO and HCN, confirming selectivity. Overall, NiTPPH and ZnTPPH are established as promising candidates for selective CO_2 and $COCl_2$ sensing. This provides a theoretical basis for developing advanced porphyrin-based materials for environmental monitoring.[28]

Furthermore, recent Density Functional Theory (DFT) investigations have explored the absorption of these industrial gases (CO_2, SO_2, NO_2) on carbon-based materials, revealing that surface modification influences adsorption strength and electronic sensitivity. Akhmetsadyk *et al.* (2023), examined SO_2 adsorption on pristine and N, GA, and Ga–N co-doped graphene using the GGA-PBE functional with a DNP basis set in DMol3, and reported weak physisorption on pristine graphene ($E_{ads} = -0.32$ eV) but much stronger chemisorption after Ga-doping, accompanied by significant electronic structure changes.[29] Similarly, Lin *et al.* (2023) investigated NO_2, SO_2, and NO gases adsorption on Janus MoSeTe monolayers decorated with Fe, Co, and Ni transition metals.[30] The findings revealed that TM-decoration converts weak physisorption on pristine MoSeTe into strong, mainly chemisorptive binding for NO_2/SO_2 (approx -2.4 eV for TM-decorated systems and $1.7–1.9$ eV for pristine MOSeTe). Faghihnasiri & Branicio (2025) used DFT to assess CO_2 *vs.* N_2 on graphene; the authors report weak physisorption with CO_2 adsorption energy of -0.168 eV ($N_2 = -0.120$ eV), *i.e.*, small intrinsic selectivity on pristine graphene.[31] However, these studies are limited either to a single gas species or to non-metal doped carbons, offering little insight into how transition-metal centers influence the simultaneous adsorption of different industrial gases.

This current research utilizes density functional theory (DFT) to investigate how phosphorus (P) doping and chromium (Cr) encapsulation enhance the adsorption and sensing performance of a single-layer porphyrin (PPR) material for CO_2, SO_2, and NO_2 gases. This work aims to investigate the performance of phosphorus-doped chromium-encapsulated porphyrin (Cr–P@PPR) material towards the adsorption of the labelled gases. The modification of porphyrin will be valuable in synergistic modulation of the electronic structure and behavior that is achieved through a combined effect of phosphorus doing chromium encapsulation, which has not been explored in previous metal-doped porphyrin-based gas sensors. This will result in the first reported Chromium-phosphorous engineered porphyrin nanostructure, enabling enhanced sensitivity and selectivity for CO_2, SO_2, and NO_2 compared to previously reported metal-doped porphyrins and other carbon materials. Cr metal creates a 3D environment and steric confinement, leading

to specific site for orbital overlap and selective trapping of the gases. The effect of surface modification by phosphorus-doping and chromium-encapsulation on the surface was determined through various computational analyses, such as geometry optimization, electronic properties (FMO and NBO analyses), visual study (QTAIM and NCI analyses), adsorption energy computation, and, lastly, the use of the selected sensor properties. This exploration opens doors for developing PPR-based gas detectors applicable to monitor operating conditions in CO_2, SO_2, and NO_2 gases.

2 Computational details

2.1 DFT approach

All software programs computationally utilized for the design and calculations of phosphorus-doped chromium-encapsulated porphyrin (Cr–P@PPR) are as follows: Gaussview 6.0.16,[32] Gaussian 16 for optimization,[33] Multiwfn software 3.7 for visualizing the reduced density gradient (RDG) and derivation of the QTAIM descriptor,[34] visual molecular dynamics (VMD) software for plotting the RDG,[35] and ChemCraft software was employed in the visualization of HOMO–LUMO electronic isosurfaces of the systems.[36]

2.1.1 Engineering of phosphorus-doped chromium-encapsulated porphyrin (Cr–P@PPR). The studied Cr–P@PPR was modeled by firstly doping the porphyrin surface with the phosphorus atom and then encapsulating it with chromium, forming phosphorus-doped chromium-encapsulated porphyrin (Cr–P@PPR), which was optimized for geometry equilibration.

2.1.2 Geometry optimization of the surface and adsorbate. Single-point energy (SPE) calculations and geometry optimizations have been performed within the framework of density functional theory (DFT), utilizing the Gaussian 16 code and GaussView 6.0.16 software. The calculations were carried out using the GENECP/LANL2DZ/Def2svp basis set and incorporating the HSEH1PBE functional due to its proven accuracy in predicting the electronic and adsorption properties of a system.[37] The HSEH1PBE hybrid functional was employed because its screened Hartree–Fock exchange improves the description of localized d-orbitals in transition-metal systems, such as Cr-based adsorbents, where conventional GGA functionals often underestimate electronic interactions. Prior studies have shown that HSE-type functionals yield reliable adsorption energies and electronic properties for gas-surface systems.[38] Grimme's D3 dispersion correction effect was included to ensure accurate treatment of long-range van der Waals interactions critical for gas-surface interactions. This consideration was consistently applied across all computations and analyses presented in this current study. For the basis sets, LANL2DZ with effective core potentials was applied to Cr to account for relativistic effects efficiently. Def2-SVP was used for lighter atoms (C, H, O, N, S) to achieve balanced accuracy in geometry optimization and adsorption studies. The GENECP combination ensures accurate treatment of the transition metal while maintaining computational efficiency.[39] The calculations herein included the quantum descriptors, natural bond orbital (NBO), the topology analysis for inter and intramolecular

interactions (QTAIM and NCI), and adsorption studies, which were integral aspects of this study.

2.1.3 Adsorption strategy of the gases (CO_2, SO_2, and NO_2) on phosphorus-doped chromium-encapsulated porphyrin. The optimization of the surface was carried out before modification, then after modification, it was optimized again to attain a stable geometry structure. The gases are positioned randomly at the center of the surface for adsorption. To ascertain the best configuration, equilibration of the surfaces close to the gases was carried out during optimization.

3 Results and discussions

3.1 Structural geometry analysis

The studied Cr–P@PPR surface and CO_2–Cr–P@PPR, NO_2–Cr–P@PPR, and SO_2–Cr–P@PPR complexes were optimized using the DFT/HSEH1PBE/LANL2DZ level of theory. Optimization plays a very important role in the computation of adsorption energy between the investigated surface and the gases (CO_2, NO_2, and SO_2). This present study involves doping the porphyrin surface with chromium and phosphorus atoms to form phosphorus-doped chromium-encapsulated porphyrin (Cr–P@PPR). Upon modification, the newly tailored surfaces were positioned to ensure the best adsorption configuration towards the adsorption of CO_2, NO_2, and SO_2 gas molecules. Upon adsorption, the resulting complexes are CO_2–Cr–P@PPR, NO_2–Cr–P@PPR, and SO_2–Cr–P@PPR corresponding to the adsorption of CO_2, NO_2, and SO_2. Fig. 1 presents the optimized structures of the gases, adsorbent, and complexes formed.

The gases shown in the figure showcase geometries that agree with previous computational research. Herein, the bonds C–O, S–O, and N–O with the bond lengths of 1.157, 1.145, and 1.193 Å are computationally intact, as they correspond to previous theoretical work.[40,41] The pictorial representation of the gases helps illustrate the increase in the bond length after adsorption. Table 1 shows the summary of the computed bond lengths during the pre- and post-adsorption. This increment in bond lengths, as observed, is nearly insignificant when compared with those obtained before adsorption. For instance, the complex CO_2–Cr–P@PPR has a bond length of 2.077 Å (Cr_{39}–N_{19}) before adsorption, and then that of 2.081 Å upon adsorption. Upon adsorption, the bonds within the surface have been observed to slightly increase and decrease, wherein the SO_2–Cr–P@PPR complex showcased a decrease. In furtherance, another decrement was observed in the NO_2–Cr–P@PPR complex. Lastly, the CO_2–Cr–P@PPR complex shows an increment and a decrement at different instances in its bond lengths. This result indicates that adsorption of the labelled gases causes slight changes in the surface morphology, thereby elucidating the presence of the mentioned gases on the adsorbent.

3.2 Electronic properties

3.2.1 FMO analysis: energy gap fluctuation and the chemical quantum descriptors. Quantum descriptors are very important parameters that enable one to understand the reactivity, stability, and conductivity of a complex. It therefore
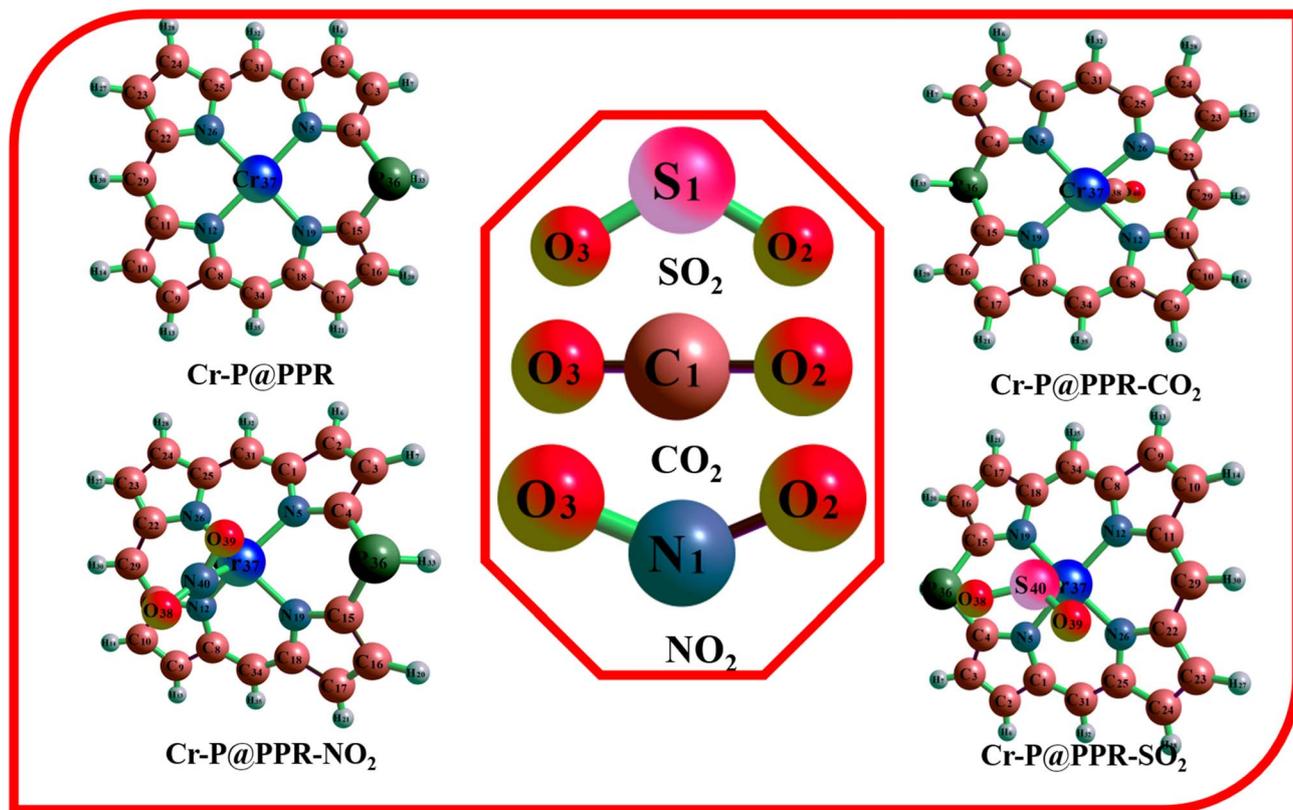
Fig. 1 Optimized structures of CO_2, SO_2, and NO_2 adsorption on the Cr–P@PPR surface, showing the configurations before and after adsorption for each gas molecule.

Table 1 Cr–N bond lengths (Å) in the Cr–P@PPR complex before and after adsorption of CO_2, SO_2, and NO_2 gas molecules, showing structural changes upon gas interaction

Complex	Bond label	Pre-adsorption	Post-adsorption
CO_2–Cr–P@PPR	$Cr_{39}–N_5$	2.090	2.081
	$Cr_{39}–N_{19}$	2.077	2.081
	$Cr–N_{12}$	2.054	2.042
	$Cr–N_{26}$	2.041	2.042
SO_2–Cr–P@PPR	$Cr–N_5$	2.090	2.068
	$Cr–N_{19}$	2.077	2.075
	$Cr–N_{12}$	2.054	2.033
	$Cr–N_{26}$	2.041	2.025
NO_2–Cr–P@PPR	$Cr–N_5$	2.090	2.062
	$Cr–N_{19}$	2.077	2.099
	$Cr–N_{12}$	2.054	2.019
	$Cr–N_{26}$	2.041	1.996

becomes a crucial approach used in computational chemistry to understand the electronic and optical properties, taking cognizance of the energies of the highest occupied orbital (E_{HOMO}) and that of the lowest unoccupied orbital (E_{LUMO}), where they are fundamentally applied in obtaining the energy gap.[42,43] The energy gap is the difference between the HOMO and the LUMO, and the results are summarized in Table 2.

The highest energy gap was observed in the complex CO_2–Cr@PPR with a value of 1.848 eV. Although the pure surface has a small energy gap of 1.297 eV, it increases upon adsorption in CO_2–Cr@PPR and SO_2–Cr@PPR. A study by Saini and Pandey (2025), that the adsorption of gases, including CO_2, resulted in a significant increase in the energy gap.[44] A decrease in the energy gap was obtained in NO_2–Cr@PPR, where it decreased to 1.071 eV. The effect of CO_2 adsorption differs from NO_2 and SO_2. This is explained by the chemical activities of the P-block elements (non-metals). The results showed higher reactivity of

Table 2 Quantum chemical descriptors of Cr–P@PPR and its gas-adsorbed complexes (CO_2, SO_2, and NO_2), with all units in electron Volt (eV), except for chemical softness (S) with a unit of eV^{-1}

Complexes	E_{HOMO} eV	E_{LUMO} eV	I_P eV	E_A eV	E_{GAP} eV	μ (eV)	χ (eV)	η (eV)	S (eV^{-1})
Cr–P@PPR	−4.352	−3.054	4.352	3.054	1.297	−3.703	3.703	0.648	0.770
CO_2–Cr@PPR	−5.269	−3.421	5.269	3.421	1.848	−4.343	4.343	0.924	0.540
SO_2–Cr–P@PPR	−5.668	−3.845	3.668	3.845	1.823	−4.757	4.757	0.911	0.548
NO_2–Cr–P@PPR	−4.749	−3.677	4.749	3.677	1.071	−4.213	4.213	0.535	0.933

the modified porphyrin surface in adsorbing gases compared to those obtained from Ammar and Badran's work (2019), whose transition metal-doped porphyrin surfaces had an energy gap within the range of 2.827–3.124 eV.[45] This implies a significant influence of the dopant on the change in the electronic state of the material. Further investigation of the stability and reactivity of the complexes and surface can be scrutinized with the help of the chemical descriptors. Improvement in the chemical reactivity and kinetic stability of the studied complexes has been achieved through the reactivity descriptors.[46] The subject encompassing the frontier molecular orbital envelops crucial information about the studied complexes and surface. These descriptors include the ionization potential (IP), electron affinity (EA), chemical softness (S), chemical potential (μ), electronegativity (X), and global hardness (η), which have been theoretically deployed to evaluate the reactivity properties of the studied complexes. The Koopmann hypothesis[47] has been applied to calculate these descriptors as shown in the following eqn (1)–(6).

$$IP = -E_{HOMO} \tag{1}$$

$$EA = -E_{LUMO} \tag{2}$$

$$\mu = -\frac{1}{2}(IP + EA) \tag{3}$$

$$X = \frac{IP + EA}{2} = -\mu \tag{4}$$

$$\eta = \frac{1}{2}(IP - EA) \tag{5}$$

$$S = \frac{1}{2\eta} \tag{6}$$

Referring to the Koopmann approximation, the ionization potential (IP) can be directly proportional to the energy of HOMO. The electron affinity (EA) has a relationship with LUMO energy. In conjunction, global hardness and the electrophilicity index account for greater stability and low reactivity of the complexes studied. The ionization potential is the energy needed for the transfer of electrons from HOMO to LUMO, and electron affinity is the energy released when molecules, atoms, etc. accept electron(s). Chemical hardness defines the tendency of a chemical species to resist electron charge transfer within its chemical environment.[48] On the other hand, knowing that chemical hardness is the direct opposite of chemical softness it means the ability of a chemical species to attract electron charge transfer. These two parameters (chemical hardness and chemical softness) depend on how firmly the atoms are held together. From Table 2, a higher global hardness value of 0.924 eV was recorded for CO_2–Cr@PPR. As chemical hardness displays small or mild resistance to electron transfer, this suggests relatively little resistance.[49] Moreover, the least value of 0.535 eV was observed in complex NO_2–Cr–P@PPR, suggesting a relatively greater resistance among its studied counterparts. Finally, the HOMO and LUMO plots showing the distribution of HOMO–LUMO for the surface before and after interaction are presented in Fig. 2.

3.2.2 NBO analysis: perturbation study. Natural bond orbital analysis plays a significant role in describing intermolecular and intramolecular interactions, arising from chemical bonds in molecules, making it an effective tool in elucidating hyperconjugation and electron density transfer from filled lone-pair electrons. According to Weinhold et al.,[50] NBO analysis provides detailed information regarding the distribution of electrons with molecular bonds that exist between atomic species. The stabilization energy (second-order perturbation energy, E^2) was theoretically calculated and expressed in eqn (7).
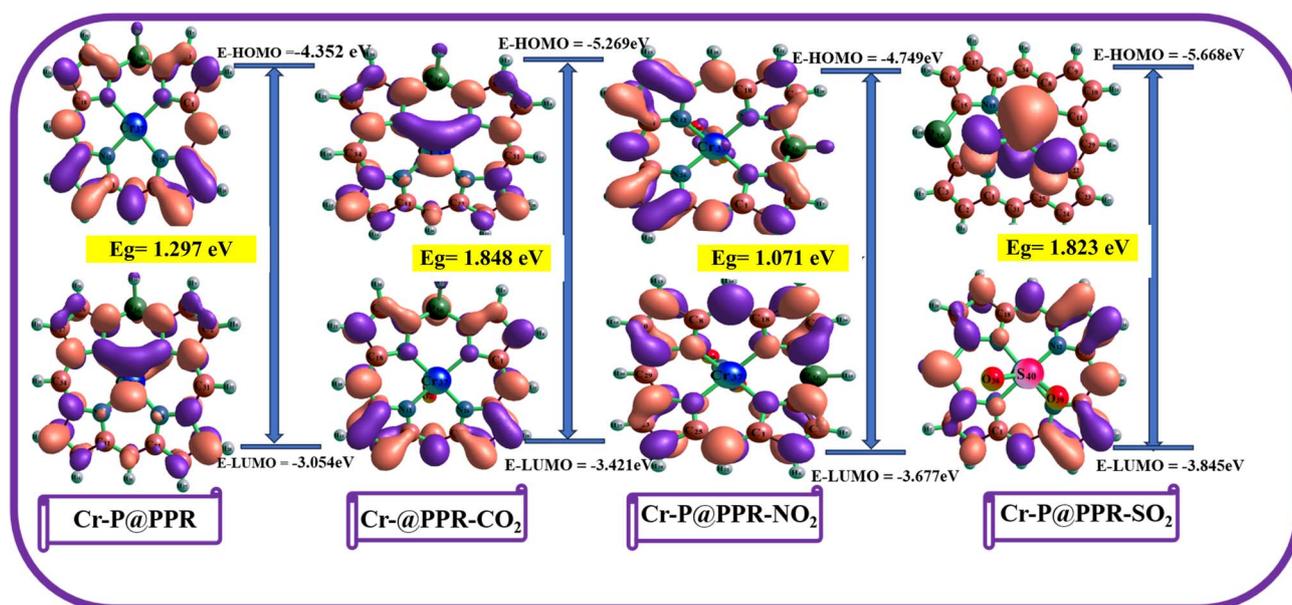

Fig. 2 The visualization of the HOMO and LUMO plots for of Cr–P@PPR, CO_2–Cr–P@PPR, NO_2–Cr–P@PPR, and SO_2–Cr–P@PPR.

Table 3 Second-order perturbation stabilization energies (E^2, kcal mol^{-1}) from NBO analysis for Cr–P@PPR and its gas-adsorbed complexes (CO_2, SO_2, and NO_2)

System	Donor	Acceptor	E^2 kcal mol^{-1}	$E(i) - E(j)$	$F(ij)$
Cr–P@ PPR	$\pi^*(2)C_1-C_2$	$\pi^*(2)C_{25}-C_{31}$	126.42	0.01	0.078
	$\pi^*(2) C_3-C_4$	$\pi^*(2)C_1-C_2$	120.53	0.01	0.073
CO_2–Cr–P@PPR	LP* (1) C_{11}	LP (1) C_{29}	320.06	0.03	0.138
	LP*(5) Cr_{37}	LP*(6) Cr_{37}	160.04	0.05	0.228
SO_2–Cr–P@PPR	LP*(1) C_{31}	LP (1) C_{25}	909.58	0.01	0.135
	LP (1) C_{11}	LP*(1) C_{29}	481.60	0.02	0.138
NO_2–Cr–P@PPR	$\pi^*(2) C_8-N_{12}$	π (2) $C_{18}-C_{34}$	168.89	0.03	0.093
	$\pi^*(2) C_{22}- N_{26}$	$\pi^*(2) C_{11}-C_{29}$	140.47	0.04	0.091

$$E^2 = \Delta E_{ij} = q_i \left(\frac{(F_{ij})^2}{E_i - E_j} \right) \qquad (7)$$

where q_i denotes the donor occupancy, $F(i,j)$ is the off-diagonal NBO Fock Matrix elements, and E_i and E_j represent the diagonal elements. Reviews from literature show that the higher the second-order perturbation of energy corresponds with the stronger the interaction between the donor and acceptor orbital, with a greater level of conjugation.[51] The summarized results of the NBO calculation for the studied surface and its complexes are presented in Table 3, illustrating charge delocalization from donor to acceptor orbitals, second-order perturbation energies, diagonal elements, and off-diagonal NBO Fock matrix elements. For the pristine Cr–P@PPR surface, electron transition occurs from donor to acceptor orbitals ($\pi^* \rightarrow \pi^*$), with a perturbation energy of 126.42 kcal mol^{-1}. Upon gas adsorption, the results reveal that SO_2 exhibits the highest stabilization energies (909.58 and 481.60 kcal mol^{-1}), indicating the strongest charge delocalization and interaction with the Cr–P@PPR surface. In comparison, CO_2 shows moderate stabilization energies (320.06 and 160.04 kcal mol^{-1}), while NO_2 displays comparatively lower values (168.89 and 140.47 kcal mol^{-1}). Specifically, for the Cr–P@PPR–NO_2 complex, charge transitions occur from $\pi^*(2)$ C8–N12 $\rightarrow \pi^*(2)$ C18–C34 and C22–N26 $\rightarrow \pi^*(2)$ C11–C29, with corresponding energies of 168.89 and 140.47 kcal mol^{-1}, respectively. Similarly, the CO_2–Cr–P@PPR complex exhibits relatively higher stabilization energies (320.06 and 160.04 kcal mol^{-1}), primarily due to charge delocalization involving lone pair $\rightarrow$ lone pair interactions.[52] These findings suggest that the Cr–P@PPR surface possesses promising adsorption characteristics for gas capture, with SO_2 forming the most stable complex, thereby demonstrating the strongest adsorption behavior compared to NO_2 and CO_2.

3.3 Visual study

3.3.1 The 3D-RDG maps analysis.
The concept of non-covalent interaction (NCI) helps to explain in detail the structural properties as well as the forces taking place during the interaction. It enables us to effectively visualize the structures, interpret, and distinguish the kinds of interactions that occur. The NCI includes the use of electron density and its gradient (RDG), thus presented as a plot and the second eigenvalues of the Hessian matrix (λ_2).[53] The forces involved here are the hydrogen bonds, electrostatic forces, and van der Waals (repulsive forces), which are elucidated using the NCI study. During this study, the interaction between the surface Cr–P@PPR was investigated to determine the non-covalent interaction and how it affects the adsorption ability of the labelled gases. Using the computational software Visual Molecular Dynamics (VMD), the NCI was viewed, and the RDG scatter plots were obtained and incorporated for the evaluation of the readings obtained through this software application. From Fig. 3, it was observed that the complex CO_2–Cr–P@PPR is characterized by a hydrogen bond, denoting a strong interaction. On the other hand, the complex SO_2–Cr–P@PPR has a constituent property of a strong repulsive force caused by steric. This distinguishable characteristic of this complex is traceable to the features of its adsorbent (gas), although the complex NO_2–Cr–P@PPR is more repulsive than attractive because of the higher steric effect.

3.3.2 Quantum theory of atoms-in-molecules (AIMs) analysis.
The theory of quantum molecules was developed to decrypt the intermolecular interaction that exists between molecules, which involves ionic bonding, van der Waals forces of attraction, and covalent bonding of structures.[54] This analysis is often carried out to determine whether these molecules can interact between species. The phrase "quantum molecular theory" is best treated with various topological parameters to validate the authenticity of the nature of interaction arising because of adsorption. These parameters include: the density of all electrons $\rho(r)$, the Lagrangian Kinetic Energy $G(r)$, Laplacian of electron density $\nabla^2\rho(r)$, potential energy density $V(r)$, Energy density $E(r)$ or $H(r)$, Eigenvalues of Hessian (λ_1, λ_2, and λ_3), Electron Localization Function (ELF), and Ellipticity of Electron Density ε.[55] Ultimately, the basis for which these analyses were carried out was to ensure the strength of the interactions at different critical points (CPs) for each of the complexes and their possible significance as captured in sensor materials. Table 4 presents these topological parameters computed at bond critical points (BCPs). Literature review shows that the expression $\rho(r) > 0.1$ is usually attributed to higher stability, which connotes the complexes studied at various CPs.[56] The reverse implication of the latter is that, for every CP having $\rho(r) < 0.1$, there will be a likelihood that such a complex may not be stable.[57] Furthermore, the density of electrons $H(r)$ is
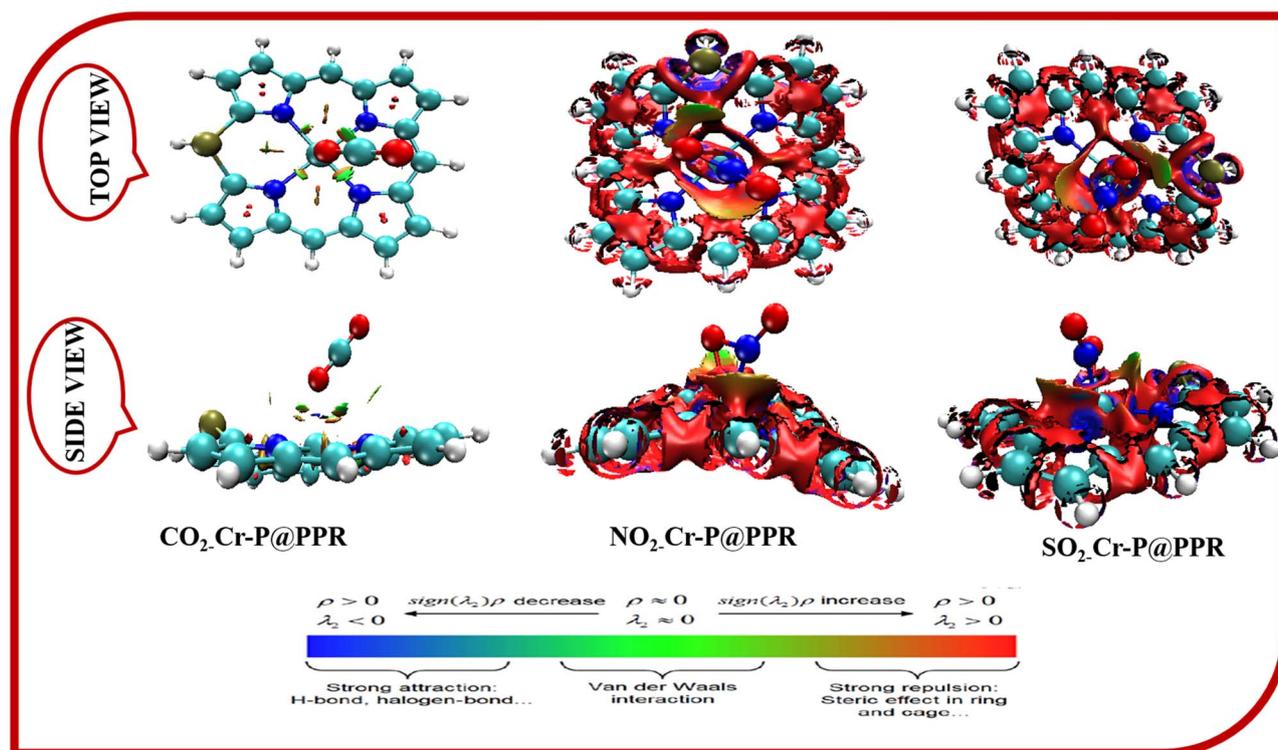
Fig. 3 The 3D RDG maps for the studied complexes display the designated colour peaks, which explain the intermolecular interaction between the modified porphyrin surface and the adsorbed gases.

responsible for the nature of interaction, which signifies that if this parameter has negative values, there is a likelihood of a covalent attraction of molecules. In furtherance, the Laplacian of Electron Density $\nabla^2 \rho(r)$ accounts elaborately on the nature of the interaction, wherein a Laplacian of Electron Density $\nabla^2 \rho(r) > 0$ and Energy Density $H(r) < 0$, indicates non-covalent interaction.[58] From Table 4, all complexes exhibit a non-covalent and partial covalent form of interaction. These properties are those found to align with sensor materials. Positive ellipticity of electron density $\varepsilon > 0$ suggests elongated electron density along the bond axis, thus signifying a polar covalent bond with some degree of ionic character.[59] The larger the positive value, the

greater the ionic contribution to the bond. This statement is significant to our case, as captured in Table 1, where the positive values show some degree of ionic character with greater ionic contribution.

3.4 Adsorption study

To gain elaborate insight into the subject of adsorption studies, the studied complexes were optimized before and after detection. On the cluster, we have the initial structural equilibration LANL2DZ as the employed basis set. Also, all computations were carried out using DFT/HSEH1PBE/LANL2DZ level of theory. The adsorption behaviors of the Cr–P@PPR surface in the detection

Table 4 The summarized result of the topological parameters computed at bonds critical points (BCPs) and calculated[a]

System	Bonds	CPs	$P(r)$	$\nabla^2 \rho(r)$	$G(r)$	$V(r)$	$K(r)$	$H(r)$	ELF	LOL	λ_1	λ_2	λ_3	λ_1/λ_3	ε
CO$_2$–Cr_P@PPR	Cr$_{37}$–O$_{39}$	67	0.378	0.258	0.538	−0.430	−0.108	0.108	0.492	0.185	−0.598	−0.574	0.376	−1.590	0.041
	N$_{26}$–C$_{22}$	63	0.420	0.308	0.749	−0.142	0.672	−0.672	0.449	0.474	0.256	−0.113	−0.113	−2.265	0.000
	C$_4$–N$_5$	68	0.299	−0.413	0.109	−0.413	0.304	−0.304	0.927	0.779	−0.579	0.275	−0.476	1.216	0.217
NO$_2$–Cr_P@PPR	Cr$_{37}$–N$_5$	71	0.969	0.525	0.102	−0.735	−0.289	0.289	0.150	0.110	0.162	0.423	−0.593	−0.273	−1.367
	C$_{15}$–P$_{36}$	68	0.133	0.184	0.132	−0.218	0.863	−0.863	0.361	0.429	−0.154	0.463	−0.124	1.242	0.242
	C$_{18}$–N$_{19}$	56	0.291	−0.578	0.172	−0.489	0.317	−0.317	0.819	0.680	−0.555	0.460	−0.483	1.149	0.150
SO$_2$–Cr_P@PPR	Cr$_{37}$–S$_{40}$	69	0.517	0.135	0.381	−0.425	0.438	−0.438	0.234	0.355	−0.693	−0.617	0.266	2.319	0.121
	N$_{26}$–C$_{22}$	64	0.297	−0.600	0.187	−0.524	0.337	−0.337	0.805	0.670	0.467	−0.568	−0.499	0.069	0.137
	C$_4$–N$_5$	57	0.310	−0.591	0.219	−0.586	0.367	−0.367	0.775	0.650	0.499	−0.579	−0.512	−0.975	0.130

[a] The units of the parameters in Table 5 are as follows: $P(r)$, e Ang^{-3}; $\nabla^2 \rho(r)$, e Ang^{-3}; λ_1, λ_2, and λ_3 have a unit of e Ang^{-5} respectively; $G(r)$ and $V(r)$ have units of eV; $H(r)$ has a unit of eV Ang^3 e^{-1}; ellipticity of electron density (ε), electron localization function (ELF) and λ_1/λ_3 are dimensionless. The unit of $G/|V|$ is Ang^3.

of CO_2, NO_2, and SO_2 have been effectively studied using the calculated adsorption energies of the studied complexes. Mathematically, the following eqn (8) was used to account for the adsorption of the various gases:

$$E_{ads} = E_{Complex} - E_{Surface} - E_{Gas} \qquad (8)$$

Various theoretical literatures assert that greater adsorption of energy is beneficial in comparative studies across different complexes.[60–62] That implies the greater the detection energy, the greater the likelihood that the adsorbent material best detects the adsorbate during the study. Although the detection energy in our case, as revealed in Table 5, shows physisorption with small values. According to their detecting abilities, the complexes follow the order: NO_2–Cr–P@PPR < SO_2–Cr–P@PPR < CO_2–Cr–P@PPR, with the detection energies recorded as 10.471, 6.503, and 4.581, respectively. Although the adsorption energies for this study showed higher physisorption, the result is comparable to the findings presented in the research of Saini and Pandey (2025). Whose result showed approximately 0.326 eV energy for the adsorption of CO_2 by metalated porphyrin material.[28] Likewise, NO_2 adsorption by porphyrin in the research of Shah *et al.* (2024) demonstrated chemisorption adsorption energy of −0.78 eV.[63] BSSE correction was performed for the systems, and the adsorption energy was observed to range from 4.589 eV (CO_2) to 10.481 eV (NO_2), which implies that gas adsorption consistently occurs *via* weak electrostatic and van der Waals forces rather than chemical bonding. The inclusion of BSSE correction increased the adsorption energies by 0.008–0.111 eV, confirming that basis set overlap has only a minor numerical impact on the computed adsorption strengths. This minor correction validates the accuracy of the LANL2DZ/Def2svp basis sets and the capacity of the HSEH1PBE functional in describing non-covalent interactions in transition-metal systems. The physisorption of these gases depends on temperature and the surface. Physisorption of a gas increases with a decrease in temperature and surface area, which is due to the formation of van der Waals forces of attraction.[64] Due to the physical nature of the adsorption of the three gases on the Cr–P@PPR surface, the investigated surface could be used for the detection of the labeled gases. This will lead to a quick recovery of the gases (reversible sensing), and reusability of the surface, as adsorption is weak. In conclusion, this surface may be suitable for detection rather than the removal of these gases. Thus, the weak yet stable physisorption highlights the potential of Cr–P@PPR for selective, reusable gas sensing applications.

3.5 Sensor properties

Detection of gases on a newly engineered surface can be further analyzed through sensor properties such as conductivity, electrical back donation, and fraction of electron transfer, and charge transfer mechanism. These properties would provide further insights into the detecting or adsorbing behaviors of the new surface. This section will therefore focus on the applicability of a Cr–P@PPR adsorbent material towards the detection of some selected gases like CO_2, SO_2, and NO_2 gas molecules.

3.5.1 Fraction of electron transfer (FET) and electrical back-donation. The usefulness of the global hardness in the realm of the adsorption mechanism cannot be overemphasized. In here, the electrical back donation has been computed using the values of the global hardness as calculated in the section on electronic properties. Generally, a good detector or sensor is one with an attribute of global hardness value greater than zero ($\eta > 0$) and a back donation less than zero ($\Delta E_{Back-donation} < 0$).[65,66] The $\Delta E_{Back-donation}$ and ΔN have been calculated using the eqn (9) and (10) respectively as follows:

$$\Delta E_{Back-donation} = -\frac{\eta}{4} \qquad (9)$$

$$\Delta N = \frac{\chi_{isolated} - \chi_{system}}{2\left(\eta_{isolated} - \eta_{system}\right)} \qquad (10)$$

As observed, the electrical back donations are all negative (see Table 6), showing the characteristic of a promising adsorbent material. The calculated back donation presented in the table was observed to be in a small range of −0.231 to −0.134 eV, elucidating that the detection of these gases on the modified surface exhibits close and similar adsorbing properties across all complexes formed. FET values are within a close range of −0.0288 to 0.1386, with the least and greatest values attributed to SO_2–Cr–P@PPR and NO_2–Cr–P@PPR, respectively.

Table 6 Summary of the sensor performance computed at DFT/B3LYP/6-31+G(d) computational method[a]

Systems	Q_t (e)	ΔN	$\Delta E_{Back-donation}$	ΔE_g	% ΔE_g
CO_2–Cr–P@PPR	1.367	0.0883	−0.231	0.425	42.483
SO_2–Cr–P@PPR	1.422	−0.0288	−0.134	−0.174	−17.425
NO_2–Cr–P@PPR	0.675	0.1386	−0.228	0.406	40.555

[a] The units of ΔE_g and $\Delta E_{back-donation}$ are in electron volt (eV). The Q_t has a unit of electron (e), and finally, the % ΔE_g has its unit in percentage. ΔN is dimensionless.

Table 5 The adsorption energy of the studied complexes in Hartree (H) and electron Volt (eV) with energies >0 eV, depicting physisorption of the gases

Complexes	$E_{Complex}$	$E_{Adsorbent}$	$E_{Adsorbate}$	E_{ads} Hartree	E_{ads}(eV)	BSSE energy	E_{ads} + BSSE (eV)
NO_2–Cr–P@PPR	−1580.741	−1375.985	−205.140	0.384	10.471	0.01004	10.481
SO_2–Cr–P@PPR	−1924.126	−1375.985	−548.380	0.239	6.503	0.1105	6.6135
CO_2–Cr–P@PPR	−1564.277	−1375.985	−188.460	0.168	4.581	0.0077	4.5887

Our result in this section agrees with those obtained in the previous section and can therefore suggest a good adsorption pattern.

Notably, Wei *et al.* (2018), in their DFT studies of gas adsorption on doped MoS_2 monolayers, specifically Ni-doped MoS_2, reported ΔE values around -0.2 eV for SO_2 adsorption, along with fractional charge transfers ΔQ in the range of approximately 0.10–0.15 e.[67] Similarly, a study using phosphorene-based sensors by Cai *et al.* (2017) shows strong NO_2 adsorption with significant charge transfer, approximately 0.10–0.20 e, and comparable adsorption energies.[68] Thus, the results from our back-donation values (-0.231 to -0.134 eV) and FET values (approximately -0.028 to 0.14) fall well within the ranges reported for established 2D-material gas-sensor platforms, supporting the viability of Cr–P@PPR surfaces as competitive sensor candidates.

3.5.2 Charge transfer mechanism. The natural charge on the gases and the newly tailored material after adsorption were considered when computing the mechanism of charge transfer (Q_t). This was calculated using eqn (11).[69] The distribution of electron density makes it feasible to investigate the charge transfer mechanism of a complex.

$$Q_t = Q_{adsorption} - Q_{isolated} \quad (11)$$

From the equation, the charge transfer, charge transfers on the gases, and that on the surface are represented by Q_t, $Q_{isolated}$, and $Q_{adsorption}$, respectively. Previous studies reported that a charge transfer from the gas to the surface is seen through the negative magnitude of charge transfer, whereas that from the surface to the gas is described by a positive charge transfer.[70] Table 6 presents the summarized result of the charge transfer. For all three complexes, positive Q_t values were obtained (see Table 6), showcasing electron transfer from the surface to the gases. As was observed, this is an indication of a good detecting material for CO_2, SO_2, and NO_2 gas pollutants. Therefore, the newly engineered phosphorus-doped chromium-encapsulated porphyrin (Cr–P@PPR) possesses a good sensitivity and selectivity towards gas adsorption.

4 Conclusions

The detection of toxic gases for investigating the potential of a newly engineered phosphorus-doped chromium-encapsulated porphyrin (Cr–P@PPR) material was carried out using the DFT/B3LYP/LANL2DZ level of theory. Various theoretical/computational analyses were carried out to inquire into the inherent properties of these materials, and the following deductions have been drawn:

(I) Detection of the CO_2, SO_2, and NO_2 gas molecules caused slight changes in the surface morphology, showing the effect of detection on the surface.

(II) Higher global hardness value of 0.924 eV in CO_2–Cr@PPR suggests a relatively smaller resistance. The least value of 0.535 eV was observed in complex NO_2–Cr–P@PPR, suggesting a relatively greater resistance among its studied counterparts.

(III) All systems showcased high perturbation energy. However, the greatest perturbation energies of 909.58 and 481.60 Kcal mol^{-1} observed for the surface upon the adsorption of SO_2 gas show that the Cr–P@PPR–SO_2 complex will be easily stabilized as compared to its studied counterparts.

(IV) AIM analysis showed that all complexes exhibit majorly non-covalent and partial covalent forms of interactions, which are found to align with sensor materials. Also, the positive values of ellipticity (ε) show some degree of ionic character with a greater ionic contribution.

(V) An increasing order of detecting strength follows: NO_2–Cr–P@PPR < SO_2–Cr–P@PPR < CO_2–Cr–P@PPR, with the detection energies recorded as 10.471, 6.503, and 4.581 eV respectively.

Author contributions

Ededet A. Eno: conceptualization, project administration and supervision. Miracle N. Ogbogu: data curation and formal analysis. Opeyemi M. Oyebanji and Morenikeji A. Ajayi: manuscript writing, editing and interpretation of data. Wrote the paper. Stephen A. Adalikwu and Ernest G. Irilochuwe: validation and visualization. Jeremiah E. Ochepo: methodology and manuscript proofreading.

Conflicts of interest

We declare no conflict of any sort.

Data availability

All data are contained within the manuscript.

Acknowledgements

References

1 I. B. Abaje, Y. Bello and S. A. Ahmad, A review of air quality and concentrations of air pollutants in Nigeria, *J. Appl. Sci. Environ. Manag.*, 2020, **24**(2), 373–379.

2 J. Lewtas, Air pollution combustion emissions: characterization of causative agents and mechanisms associated with cancer, reproductive, and cardiovascular effects, *Mutat. Res., Rev. Mutat. Res.*, 2007, **636**(1–3), 95–133.

3 D. K. Saini, S. K. Garg and M. Kumar, Major air pollutants and their effects on plant and human health: a review, *Plant Arch.*, 2019, **19**(2), 09725210.

4 R. Saidur, H. H. Masjuki, M. Y. Jamaluddin and S. Ahmed, Energy and associated greenhouse gas emissions from household appliances in Malaysia, *Energy Policy*, 2007, **35**(3), 1648–1657.

5 S. Ozgen, S. Cernuschi and S. Caserini, An overview of nitrogen oxides emissions from biomass combustion for domestic heat production, *Renew. Sustain. Energy Rev.*, 2021, **135**, 110–113.

6 W. C. Clark, J. Jäger, J. Cavender-Bares and N. M. Dickson, *Acid Rain, Ozone Depletion, and Climate Change: an Historical Overview*, 2001.

7 H. W. T. Mapoma, C. Tenthani, M. Tsakama and I. B. M. Kosamu, Air quality assessment of carbon monoxide, nitrogen dioxide and sulfur dioxide levels in Blantyre, Malawi: a statistical approach to a stationary environmental monitoring station, *Afr. J. Environ. Sci. Technol.*, 2014, **8**(6), 330–343.

8 S. Prasad, L. Zhao and J. Gomes, Methane and natural gas exposure limits, *Epidemiology*, 2011, **22**(1), S251.

9 E. Wigenstam, L. Elfsmark, A. Bucht and S. Jonasson, Inhaled sulfur dioxide causes pulmonary and systemic inflammation leading to fibrotic respiratory disease in a rat model of chemical-induced lung injury, *Toxicology*, 2016, **368**, 28–36.

10 D. B. Peden, Mechanisms of pollution-induced airway disease: *in vivo* studies, *Allergy*, 1997, **52**, 37–44.

11 B. Z. Simkhovich, M. T. Kleinman and R. A. Kloner, Air pollution and cardiovascular injury: epidemiology, toxicology, and mechanisms, *J. Am. Coll. Cardiol.*, 2008, **52**(9), 719–726.

12 R. D. Brook, Cardiovascular effects of air pollution, *Clin. Sci.*, 2008, **115**(6), 175–187.

13 L. Curtis, W. Rea, P. Smith-Willis, E. Fenyves and Y. Pan, Adverse health effects of outdoor air pollutants, *Environ. Int.*, 2006, **32**(6), 815–830.

14 S. B. Sharma, S. Jain, P. Khirwadkar and S. Kulkarni, The effects of air pollution on the environment and human health, *Indian J. Res. Pharm. Biotechnol.*, 2013, **1**(3), 391–396.

15 P. M. Irving and J. E. Miller, Productivity of field-grown soybeans exposed to acid rain and sulfur dioxide alone and in combination, *Agron. J.*, 1981, **10**(4), 473–478.

16 A. Singh and M. Agrawal, Acid rain and its ecological consequences, *J. Environ. Biol.*, 2007, **29**(1), 15.

17 P. N. Sudha, K. Sangeetha, K. Vijayalakshmi and A. Barhoum, Nanomaterials history, classification, unique properties, production and market. in *Emerging Applications of Nanoparticles and Architecture Nanostructures*, Elsevier, 2018, pp. 341–384.

18 J. K. Patel, A. Patel and D. Bhatia, Introduction to nanomaterials and nanotechnology. in *Emerging Technologies for Nanoparticle Manufacturing*, Cham, Springer Int Publ, 2021, pp. 3–23.

19 M. A. Ratner and D. Ratner, *Nanotechnology: A Gentle Introduction to the Next Big Idea*, Upper Saddle River, Prentice Hall Prof, 2003.

20 J. Shen, Y. Zhu, H. Jiang and C. Li, 2D nanosheets-based novel architectures: synthesis, assembly and applications, *Nano Today*, 2016, **11**(4), 483–520.

21 S. Saha, S. Bansal and M. Khanuja, Classification of nanomaterials and their physical and chemical nature, in *Nano-enabled Agrochemicals in Agriculture*, Academic Press, 2022, pp. 7–34.

22 A. Mazumder, S. Bhattacharya and C. Bhattacharjee, Role of nano-photocatalysis in heavy metal detoxification, in *Nanophotocatalysis and Environmental Applications: Detoxification and Disinfection*, Elsevier, 2020, pp. 1–33.

23 W. Ramadan, Y. AlSalka, O. Al-Madanat and D. W. Bahnemann, Synthesis of magnetic ferrite and TiO_2-based nanomaterials for photocatalytic water splitting applications, in *Synthesis and Applications of Nanomaterials and Nanocomposites*, Singapore, Springer Nature Singapore, 2023, pp. 293 - 329.

24 J. V. Gajjar and D. R. Roy, Porphyrin and its co-doped complex-based sensor devices for nitrogen and sulfur containing environmental toxic gases, *IEEE Sens. J.*, 2024, **24**(7), 9411–9418.

25 J. Yan, B. Zhang, S. Guo and Z. Wang, Porphyrin-based nanoporous organic polymers for adsorption of carbon dioxide, ethane, and methane, *ACS Appl. Nano Mater.*, 2021, **4**(10), 10565–10574.

26 Y. Hong, V. Rozyyev and C. T. Yavuz, Alkyl-linked porphyrin porous polymers for gas capture and precious metal adsorption, *Small Sci.*, 2021, **1**(6), 2000078.

27 H. Van Ngoc and K. D. Pham, First-principles study on N_2, H_2, O_2, NO, NO_2, CO, CO_2, and SO_2 gas adsorption properties of the Sc_2CF_2 monolayer, *Phys. E*, 2022, **141**, 115–162.

28 L. K. Saini and M. Pandey, Porphyrin-based gas sensors: a computational investigation of CO_2 and $COCl_2$ detection using pure and metallic derivatives, *Phys. Scr.*, 2025, **100**(7), 075922.

29 D. Akhmetsadyk, A. Ilyin, N. Guseinov and G. Beall, Adsorption of SO_2 molecule on pristine, N-, Ga-doped and Ga–N co-doped graphene: a DFT study, *Computation*, 2023, **11**(12), 235.

30 L. Lin, C. Xue, X. Li, H. Tao and L. Su, Adsorption and sensing of NO_2, SO_2, and NH_3 on a Janus MoSeTe monolayer decorated with transition metals (Fe, Co, and Ni): a first-principles study, *Langmuir*, 2023, **39**(36), 12662–12670.

31 M. Faghihnasiri and P. S. Branicio, Selective adsorption of CO_2 over N_2 on graphene: insights from first-principles calculations, *J. Phys. Chem. C*, 2025, **129**(5), 2851–2864.

32 G. Qu, Z. Ma and T. Jia, Influence of hydroxyl groups on the oxidative reaction characteristics of active groups in lignite at room temperature, *ACS Omega*, 2024, **9**(14), 16237–16248.

33 J. Zhang and T. Lu, Efficient evaluation of electrostatic potential with computerized optimized code, *Phys. Chem. Chem. Phys.*, 2021, **23**(36), 20323–20328.

34 A. R. Kumar, L. Ilavarasan, G. S. Mol, S. Selvaraj, M. Azam, P. Jayaprakash, *et al.*, Spectroscopic (FT-IR, FT-Raman, UV–Vis and NMR) and computational (DFT, MESP, NBO, NCI, LOL, ELF, RDG and QTAIM) profiling of 5-chloro-2-hydroxy-3-methoxybenzaldehyde: a promising antitumor agent, *J. Mol. Struct.*, 2024, **1298**, 136–974.

35 T. Mackoy, B. Kale, M. E. Papka and R. A. Wheeler, viewSq, a Visual Molecular Dynamics (VMD) module for calculating, analyzing, and visualizing X-ray and neutron structure factors from atomistic simulations, *Comput. Phys. Commun.*, 2021, **264**, 107–881.

36 R. A. Massoud and M. A. Makhyoun, Theoretical study of the interaction of ethanol with the (3,5-dimethylpyrazole-N_2)(N-salicylidenephenyl-alaninato-O,N,O′) copper(II) complex, *J. Struct. Chem.*, 2019, **60**, 882–889.

37 M. R. Poopari, Z. Dezhahang and Y. Xu, Stereochemical properties of multidentate nitrogen donor ligands and their copper complexes by electronic CD and DFT, *Chirality*, 2016, **28**(7), 545–555.

38 S. Ghoshal, P. Roy, A. Pramanik and P. Sarkar, Ru/Rh catalyzed selective hydrogenation of CO_2 to formic acid: a first principles microkinetics analysis, *Catal. Sci. Technol.*, 2022, **12**(23), 7219–7232.

39 M. Abdel-Megid, O. M. Adly, M. A. Ibrahim and R. Fouad, New metal complexes based on chromone and triazine moieties as potential antitumor agents: full structural elucidation, theoretical calculations, and biological studies, *Appl. Organomet. Chem.*, 2025, **39**(6), e70202.

40 Q. Yang, D. Liu, C. Zhong and J. R. Li, Development of computational methodologies for metal–organic frameworks and their application in gas separations, *Chem. Rev.*, 2013, **113**(10), 8261–8323.

41 Y. Zhou, *Dilithium and Disodium Salts of Pseudoephedrine-Derived Myers Enolates: Stereoselectivity and Mechanism of Alkylation [dissertation]*, Ithaca (NY), Cornell Univ, 2019.

42 B. A. Ademola, First-Principles Density Functional Theory Studies of the Structural and Electronic Properties of Prodigiosin as a Cancer Drug, PhD Thesis, African University of Science and Technology, Abuja, 2019.

43 H. Hadi, H. Louis, T. E. Gber and F. O. Ogungbemiro, Molecular modeling of the structural, electronic, excited state dynamic, and photovoltaic properties of oligomers of n-corannulene (n = 1–4), *Heliyon*, 2023, **9**(10), e2230.

44 H. Y. Ammar and H. M. Badran, Effect of CO adsorption on properties of transition metal doped porphyrin: a DFT and TD-DFT study, *Heliyon*, 2019, **5**(10), e02540.

45 J. Abdul Nasir, A. Munir, N. Ahmad, T. U. Haq, Z. Khan and Z. Rehman, Photocatalytic Z-scheme overall water splitting: recent advances in theory and experiments, *Adv. Mater.*, 2021, **33**(52), 2105–2195.

46 A. U. Hassan and S. H. Sumrra, Exploration of pull–push effect for novel photovoltaic dyes with A–π–D design: a DFT/TD-DFT investigation, *J. Fluoresc.*, 2022, **32**(6), 1999–2014.

47 R. G. Pearson, Chemical hardness and density functional theory, *J. Chem. Sci.*, 2005, **117**, 369–377.

48 J. Wang, L. N. Guo, W. M. Lin, J. Chen, S. Zhang, T. T. Zhen and Y. Y. Zhang, The effects of graphene content on the corrosion resistance, and electrical, thermal and mechanical properties of graphene/copper composites, *New Carbon Mater.*, 2019, **34**(2), 161–169.

49 R. K. Castellano, Progress toward understanding the nature and function of CH···O interactions, *Curr. Org. Chem.*, 2004, **8**(10), 845–865.

50 M. Khalid, G. Wu, A. Umber, M. Khan, A. A. Braga, N. Alhokbany and S. C. Ojha, Impact of extended π-conjugated acceptor moieties on non-linear optical behavior in polar medium for designed 4,4-dimethyl-4H-indeno[1,2-b]thiophene-based materials, *J. Mol. Liq.*, 2024, **401**, 124608.

51 B. Szcześniak, J. Choma and M. Jaroniec, Gas adsorption properties of graphene-based materials, *Adv. Colloid Interface Sci.*, 2017, **243**, 46–59.

52 A. Otero-De-La-Roza, E. R. Johnson and J. Contreras-García, Revealing non-covalent interactions in solids: NCI plots revisited, *Phys. Chem. Chem. Phys.*, 2012, **14**(35), 12165–12172.

53 C. Tantardini, A Study of Chemical Bonding through Quantum Chemical Topology, PhD Thesis, Skolkovo Institute of Science and Technology, 2020.

54 M. R. Xavier, M. M. Marinho, M. S. Julião, E. S. Marinho, F. W. Almeida-Neto, K. K. de Castro, J. P. da Hora, M. N. da Rocha, A. C. Barreto, G. D. Saraiva and P. N. Bandeira, Structural, topological, vibrational, and electronic analysis, and ADMET study of methyl-2-(4-isobutylphenyl) propanoate, *J. Mol. Struct.*, 2024, **1309**, 138019.

55 A. J. Irving, Geochemical and High-Pressure Experimental Studies of Xenoliths, Megacrysts and Basalts from Southeastern Australia, *PhD Thesis*, Canberra, Aust Natl Univ, 1971.

56 S. J. Grabowski, What is the covalency of hydrogen bonding?, *Chem. Rev.*, 2011, **111**(4), 2597–2625.

57 A. M. Donald, A. H. Windle and S. Hanna, *Liquid Crystalline Polymers*. Cambridge, Cambridge Univ Press, 2006.

58 K. S. Kim, P. Tarakeshwar and J. Y. Lee, Molecular clusters of π-systems: theoretical studies of structures, spectra, and origin of interaction energies, *Chem. Rev.*, 2000, **100**(11), 4145–4186.

59 Y. Shah, M. T. Hussain, A. Mansha and M. R. S. A. Janjua, Exploring the potential of quinacridone-porphyrin-based materials for nitrogen oxides sensing: quantum chemical design, mechanism and future prospects, *Adsorption*, 2024, **30**(8), 2053–2067.

60 K. R. S. Chandrakumar and S. K. Ghosh, Alkali-metal-induced enhancement of hydrogen adsorption in C_{60} fullerene: an *ab initio* study, *Nano Lett.*, 2008, **8**(1), 13–19.

61 E. Mete, M. Yortanlı and M. F. Danışman, A van der Waals DFT study of chain length dependence of alkanethiol adsorption on Au(111): physisorption *vs.* chemisorption, *Phys. Chem. Chem. Phys.*, 2017, **19**(21), 13756–13766.

62 Y. Guo, K. Xu, C. Wu, J. Zhao and Y. Xie, Surface chemical modification for engineering the intrinsic physical properties of inorganic two-dimensional nanomaterials, *Chem. Soc. Rev.*, 2015, **44**(3), 637–646.

63 N. Mercier, S. Poiroux, A. Riou and P. Batail, Unique hydrogen bonding correlating with a reduced band gap and phase transition in the hybrid perovskites $(HO(CH_2)_2NH_3)_2PbX_4$ (X = I, Br), *Inorg. Chem.*, 2004, **43**(26), 8361–8366.

64 R. Meenakshi, Spectral investigations, DFT-based global reactivity descriptors, inhibition efficiency and analysis of 5-chloro-2-nitroanisole as π-spacer with donor–acceptor variations effect for DSSC performance, *J. Mol. Struct.*, 2017, **1127**, 694–707.

65 R. Vuilleumier and M. Sprik, Electronic properties of hard and soft ions in solution: aqueous Na$^+$ and Ag$^+$ compared, *J. Chem. Phys.*, 2001, **115**(8), 3454–3468.

66 H. Wei, Y. Gui, J. Kang, W. Wang and C. Tang, A DFT study on the adsorption of H$_2$S and SO$_2$ on Ni-doped MoS$_2$ monolayer, *Nanomaterials*, 2018, **8**(9), 646.

67 Y. Cai, G. Zhang and Y. W. Zhang, Charge transfer and functionalization of monolayer InSe by physisorption of small molecules for gas sensing, *J. Phys. Chem. C*, 2017, **121**(18), 10182–10193.

68 J. Z. Ou, W. Ge, B. Carey, T. Daeneke, A. Rotbart, W. Shan, *et al.*, Physisorption-based charge transfer in two-dimensional SnS$_2$ for selective and reversible NO$_2$ gas sensing, *ACS Nano*, 2015, **9**(10), 10313–10323.

69 A. M. Gutiérrez-Vílchez, C. V. Ileperuma, V. Navarro-Pérez, P. A. Karr, F. Fernández-Lázaro and F. D'Souza, Excited Charge Transfer Promoted Electron Transfer in all Perylenediimide Derived, Wide-Band Capturing Conjugates: A Mimicry of the Early Events of Natural Photosynthesis, *ChemPlusChem*, 2024, **89**(11), e202400348.

70 D. Cappelletti, E. Ronca, L. Belpassi, F. Tarantelli and F. Pirani, Revealing charge-transfer effects in gas-phase water chemistry, *Acc. Chem. Res.*, 2012, **45**(9), 1571–1580.